JOURNAL OF SPACECRAFT AND ROCKETS
Vol. 33, No. 6, November–December 1996

Navier–Stokes Heating Calculations for Benchmark Thermal Protection System Sizing

David R. Olynick* and W. D. Henline†
NASA Ames Research Center, Moffett Field, California 94035-1000

A study was carried out to identify, select, and benchmark simulation techniques needed for thermal protection material selection and sizing for reusable launch vehicles. Fully viscous, chemically reacting, Navier–Stokes solutions for the flow around a sphere are generated and compared using three different flow solvers. The effects of grid resolution, algorithm, transport modeling, and surface boundary conditions on the magnitude and convergence of the predicted heat transfer rate are examined. A third-order Van Leer inviscid upwind flux formulation was found to be a good method for surface heat transfer predictions. A number of three-dimensional, chemically reacting, Navier–Stokes flow solutions are generated for the nose of a single-stage-to-orbit rocket at angle of attack. A methodology for thermal protection system material selection is demonstrated. The strong influence of thermal protection system material selection on predicted heat transfer rates and surface temperatures is demonstrated. Further, it is shown that the changes in surface emissivity and catalycity at the interfaces between different thermal protection system concepts can produce large jumps in the predicted surface temperature. These gradients must be accounted for in the thermal protection system and vehicle design process.

Nomenclature

c_s	= mass fraction for species s
D	= reference diffusion coefficient, m^2/s
$\mathcal{D}_{ij}$	= multicomponent diffusion coefficient, m^2/s
E	= activation energy for surface catalysis, K
F_i	= diffusion factor for species i
h_s	= enthalpy of species s, m^2/s^2
j_s	= diffusion mass flux of species s, kg/m^{2}s
K_w	= first-order reaction rate at wall, m/s
k	= Boltzmann constant, J/K
$\mathcal{M}$	= molecular weight of gas mixture
m_s	= mass of species s
n_s	= number of species
q_c	= total convective heat flux, W/cm^2
$\%\Delta q_c$	= percent change in q_c per iteration
T_w	= wall temperature, K
V_∞	= freestream velocity, m/s
x_s	= mole fraction of species s
Z_s	= bifurcation mass fraction for species s
γ_s	= fraction of species s consumed on surface
Δ_w	= surface cell height, m
ϵ	= surface emissivity
η	= normal direction component
κ	= thermal conductivity of gas
μ_1, μ_2	= weights used in bifurcation approximation
ρ	= mixture density, kg/m^3
σ	= Stefan–Boltzmann constant, W/cm^{2}K^4

Introduction

LESS expensive access to space has been identified as important to meeting NASA's and the nation's future needs. Thus, studies have been undertaken to determine how this goal can be met in a timely and efficient manner.[1] An important component of these studies is numerical simulation, which is utilized in all facets of the design process. These simulations include system studies to determine the size and cost of potential vehicles, detailed computational analysis of aerodynamic performance, structural characteristics, and propulsion system performance.

A critical subsystem for the design of a reusable launch vehicle (RLV) is the thermal protection system (TPS). The TPS protects the RLV from the intense heat loads experienced during re-entry. For instance, the Space Shuttle, which is currently the only operational example of an RLV, employs a system of ceramic tiles and blankets that insulate the underlying structure from the heat load experienced during re-entry.

A few factors that influence the design of a TPS are weight, thermal and aerodynamic loads, operation costs, and durability. The weight of the TPS is mostly a function of the type of TPS selected such as ceramic or metallic and the heat load, which is the heat transfer rate integrated vs time over the trajectory. For the Shuttle, developing a working system that had a reasonable weight was the major design driver. The issues of operation cost and durability did not figure prominently in the design. This is reflected in the original Shuttle TPS, which was both fragile and expensive to maintain.

The design of a re-entry vehicle is a highly coupled and iterative process. For example, the design of a TPS requires the calculation of thermal and aerodynamic loads. To calculate the thermal and aerodynamic loads a vehicle shape and trajectory are needed. The type of trajectory that can be flown is influenced by such things as cross range requirements, the aerodynamic performance of the vehicle, structural load limits, and TPS temperature limits. Because of the highly coupled nature of the RLV design problem, critical subsystem requirements in one area can drive the design of the entire vehicle. For example, the Shuttle trajectory was shaped to delay the onset of turbulent flow. Transition to turbulence early in the trajectory greatly increases the heat load, which drives up the weight of the TPS.

The focus of this paper is the coupling between the TPS and re-entry flow environment and its effects on TPS design. The work presented is a small part of an ongoing effort to develop a state-of-the-art methodology for assessing TPS requirements for future access-to-space vehicles.[2–4] The philosophy of this methodology is to include the best possible characterization of the flow environment and detailed modeling of the coupling between the flowfield and thermal protection material response during atmospheric entry.

Present application of this philosophy for an RLV employing a ceramic/blanket TPS[3,4] is to discretize the trajectory into five to six points. It is assumed that the shape of the vehicle and trajectory are known a priori. The trajectory points are chosen to capture the shape

Received Aug. 18, 1995; revision received April 15, 1996; accepted for publication April 18, 1996.

*Research Scientist, Reacting Flow Environments Branch, MS 230-2. Member AIAA.

†Research Scientist, Reacting Flow Environments Branch, MS 230-2. Senior Member AIAA.

of the heat transfer vs time curve. At a trajectory condition assumed to be near peak heating, a flow solution is generated using a chemically reacting Navier–Stokes flow solver with a conservative surface boundary condition such as a fully catalytic radiative equilibrium wall. The predicted surface temperatures from the flow calculation are used to map the selected TPS onto the vehicle's surface according to the maximum reuse temperature limits of the selected TPS concepts. For example, in this work, advanced flexible reusable surface insulation (AFRSI) blankets were applied in areas where the maximum surface temperatures during entry were less than 922 K. After the surface is mapped, Navier–Stokes solutions are generated down the trajectory. Best available data for the TPS surface properties, catalyticity, and emissivity are employed to model the fluid–surface interface in the calculation. The Navier–Stokes calculations provide an aerothermal database, which is used as input into a one-dimensional conduction code. The one-dimensional conduction code is used to size the TPS.

The output of the methodology just described is a benchmark TPS sizing. At present, the methodology is very resource intensive. Thus, only one benchmark sizing would be generated during the design of a vehicle. It is hoped that these types of calculations will provide a sanity check to the results of sizing calculations generated using simpler engineering methods. However, with expanding computational resources, this type of calculation will become the engineering method of the future.

The impact of accurate coupled numerical simulations of the TPS and flow environment are reduced TPS weight, reduced design cycle time, reduced design risk, and more efficient use of experimental resources such as arc jets and wind tunnels. For the Mars/Pathfinder project, the methodology described has been used in the design of the vehicle's aeroshell.[5] The resulting computations have been used to reduce the number of arc jet tests and size the vehicle's heat shield.

Some present weaknesses of applying the present approach to an RLV type calculation are as follows. First, using only five to six points may not be adequate to resolve the heat load. In the Mars/Pathfinder calculations,[5] 20 calculations were carried out along the trajectory. This type of resolution was possible because the calculations were axisymmetric. Second, a one-dimensional conduction model may not be adequate for TPS concepts other than blankets and tiles. However, these weaknesses do not affect the validity of the philosophy behind benchmark sizing. More trajectory points will be employed as the efficiency in generating the solutions and the speed of computers improves. Also, more complex conduction models can be employed to model TPS concepts where a one-dimensional conduction model is inadequate.

The major objective of the present paper is to identify, develop, and benchmark simulation techniques needed for optimum TPS sizing of RLVs. To minimize TPS weight, an accurate prediction of a heat load during atmospheric entry is required. Thus, the focus of this work is to assess how present methodologies affect heat transfer rates and to select appropriate models for the benchmark TPS sizing in Refs. 3 and 4. However, because of computational resource limitations, the fidelity of the methodology will be balanced against the resources required to obtain the level of fidelity.

For complex, three-dimensional flow around an RLV, a multitude of flow phenomena must be resolved. Some phenomena that must be captured are strong bow shocks, shock impingement, separated flow, and momentum, thermal, and diffusion boundary layers. Since the number of grid points that can be employed in a given simulation is limited, the effects of grid resolution and distribution on predicted heat transfer rates are studied. To model the inviscid fluxes, a one-dimensional upwind flux formulation is employed. Some examples of upwind schemes are Roe, Van Leer, and Steger–Warming. Each of these methods[6] has a characteristic numerical dissipation that is grid dependent. Unfortunately, numerical heat transfer predictions are very sensitive to numerical dissipation. Therefore, several upwind schemes are investigated and their effects determined. Energy from the inviscid portion of the flow is transferred to a vehicle's surface via the momentum, thermal, and diffusion boundary layers. The amount of energy arriving at the surface determines the heat transfer rate. Thus, the numerical modeling of the viscosity, gas thermal conductivity, and diffusion coefficients impacts the predicted heat transfer. Therefore, in this work, transport modeling effects are examined.

As described, three-dimensional calculations are very computationally intensive. Because a number of flow solutions along the trajectory must be generated to size the TPS, the total computational cost of the trajectory analysis can be quite large. To assess these costs, the numerical convergence rate of the heat transfer rate is examined as a function of grid spacing and inviscid flux formulation for various sphere configurations.

Finally, at the fluid–TPS interface, reradiation and surface recombination strongly influence the local heat transfer rate and surface temperature. The magnitudes of these phenomena are a function of TPS material properties such as emissivity and surface catalycity. A typical TPS design for an RLV uses a number of materials.[7] Discontinuities in the material properties at the interfaces between different TPS concepts can produce large temperature gradients. These gradients can thermally shock the structure producing large stresses, which must be accounted for in the vehicle design. Further, the large jumps in temperature can result in maximum temperatures that exceed the limits of a given TPS concept. Some effects of TPS material selection on heat transfer and thermal shock are illustrated by considering the three-dimensional flow around the nose of a single stage to orbit (SSTO) rocket. The nose was mapped with three materials, and the effects on surface temperature of varying the emissivity and catalycity are demonstrated.

Procedure

Fluid Flow Governing Equations

In this study, a set of governing equations was chosen that is appropriate for a Shuttle-like entry heating environment.[8] It is expected that the next generation of access-to-space vehicles will operate in a similar entry envelope. Thus, a set of the Navier–Stokes equations employing finite rate chemistry is solved that includes five species equations (N_2, O_2, NO, N, O), two momentum equations, and one energy equation. The translational, rotational, and vibrational energy modes of the various species are characterized by one temperature. Five species and a one temperature thermal model were employed because in the thermal boundary layer near the surface the internal modes are near equilibrium, and most of the ions are recombined. Therefore, thermal nonequilibrium and ionization have a minimal impact on the predicted heat transfer rate.

The multispecies Navier–Stokes equations just described are solved using a number of numerical techniques. For validation purposes, comparisons of flow solutions are made using three codes, GASP,[9] LAURA,[10,11] and GIANTS.[12,13] A brief description of the codes is as follows. LAURA and GASP are three-dimensional flow solvers, and GIANTS is a two-dimensional/axisymmetric code. Each code uses an implicit formulation to march the Navier–Stokes equations in time to a steady-state solution. GASP employs a three-factor approximate factorization scheme, LAURA uses a point-implicit algorithm and GIANTS employs a Gauss–Seidel line relaxation technique. The implicit formulation determines how fast a converged flow and heating solution is obtained. Thus, comparisons of the relative numerical efficiency of GASP and GIANTS for heat transfer are made in this study.

Since the solutions are marched to a steady state, differences in the flow solutions result from the modeling of the explicit portion of the equations. GASP, GIANTS, and LAURA each employ central differences with similar stencils to calculate the viscous fluxes. However, a variety of upwinding techniques are used in the methods to determine the inviscid fluxes. GASP offers the choices of Van Leer, Roe, or Steger–Warming approximate Riemann solvers with MUSCL variable extrapolation. LAURA employs a modified Roe scheme with total variation diminishing (TVD) flux limiters. Finally, GIANTS uses a modified Steger–Warming scheme with MUSCL variable extrapolation. Details of these methods can be found in Refs. 6 and 9–13. Each upwinding technique has a different amount of numerical dissipation, which affects the predicted heat transfer rate. Thus, numerical heat transfer rates are compared employing a number of upwinding techniques. Finally, numerical heat transfer is sensitive to grid resolution and distribution. Thus,

to determine these effects, flow solutions around hemispheres of varying nose radii are generated on a number of grids.

Transport Models and Boundary Conditions

The mixture rules for the viscosity and translational and vibrational conductivity used in this work are based on the formulations of Gnoffo[11] and Gupta et al.[14] The cross section data by Yos found in Refs. 11 and 14 have been reviewed and updated to improve the collision modeling.[15] This basic model is used in LAURA and GIANTS and was adapted into GASP for this study. In LAURA, the multicomponent diffusion is treated using Fick's law with a diffusion coefficient for each species.[16] A disadvantage of the method is that it does not conserve mass. Thus, a bifurcation approximation is used to represent the multicomponent diffusion coefficients.[17] This methodology has been incorporated into GASP and GIANTS. The bifurcation method has been shown to compare favorably with exact resolution of Stefan–Boltzmann multicomponent diffusion equations.[17,18] However, the computational cost of the method is much less than solving the exact equations. For the purposes of comparison, numerical predictions of the heat transfer are generated using Wilke's[19] semiempirical mixing rule with curve fits for the species viscosities given by Blottner et al.[20] and a constant Schmidt number. This methodology is commonly used in many hypersonic flow applications.[13]

Multicomponent diffusion coefficients are treated using a bifurcation approximation in the following manner:

$$\mathcal{D}_{ij} = (\bar{D}/F_i F_j) \tag{1}$$

where

$$\bar{D} = \mathcal{D}_{N_2N_2} \tag{2}$$

The diffusion factors used in this study have been determined using a nonlinear least squares curve fit of the updated binary diffusion coefficient data,[14,15] and the curve fit values of F_i are listed in Table 1. The diffusion factors are assumed constant because they are fairly insensitive to changes in pressure and temperature, and the temperature and pressure dependence are lumped into the reference diffusion coefficient.

The diffusive mass flux of species s in the η direction is determined in a form similar to Fick's law as[17]

$$j_s = -\frac{\rho \bar{D} \mu_2}{\mathcal{M}\mu_1}\frac{\partial Z_s}{\partial \eta} \tag{3}$$

where $\mathcal{M}$ is molecular weight of the gas mixture. Here, μ_1, μ_2, and Z_s are defined as

$$\mu_1 = \sum_{s=1}^{ns} x_s F_s \qquad \mu_2 = \sum_{s=1}^{ns} \frac{\mathcal{M}_s x_s}{F_s} = \mathcal{M}\sum_{s}^{ns}\frac{c_s}{F_s} \tag{4}$$

$$Z_s = \mathcal{M}_s x_s / F_s \mu_2$$

It can be shown from these definitions that the summation of j_s over all of the species is equal to zero.

The following boundary conditions are used in the study. First, a no-slip condition is assumed for the velocity at the surface. Second, the energy balance at the fluid–surface interface is modeled using a radiative equilibrium wall. This equation, assuming a bifurcation approximation for the transport model, is given as[21]

$$\kappa\frac{\partial T}{\partial \eta} + \sum_{s}^{ns}\left(\rho D^* h_s \frac{\partial Z_s}{\partial \eta}\right) = \sigma \epsilon T_w^4 \tag{5}$$

Table 1 Species diffusion factors

Species	F_i
N_2	1.0
O_2	1.06279
NO	1.03073
N	0.580012
O	0.63559

where

$$D^* = \bar{D}(\mu_2/\mathcal{M}\mu_1)$$

In the preceding equation, the diffusion of energy to the surface, which is driven by surface catalycity and the emissivity, is dependent on the TPS concept at a given surface location.

The surface catalycity is modeled using first-order reaction rates. Thus, the mass flux at the wall can be related to the rate of diffusion toward the surface as

$$\left(\rho D^* \frac{\partial Z_s}{\partial \eta}\right)_w = (\rho_s K_s)_w = \rho_s \gamma_s \sqrt{\frac{kT_w}{2\pi m_s}} \tag{6}$$

where γ_s is curve fit as a function of temperature as

$$\gamma_s = Ce^{-E/T_w} \tag{7}$$

Curve fits for γ_s of this form for reaction cured glass are given in Ref. 22.

Results

The effects on heat transfer of a number of flow models (transport, upwind flux formul formulation) are considered. Thus, to enable parametric studies, most of the calculations are performed on hemispheres of various nose radii. A typical grid for the calculations employed a grid with 31 points along the body and 81 points normal to the body. The flow conditions for the sphere calculations are given in Table 2. The conditions at 1000 s correspond to peak heating for a Shuttle-like entry of winged SSTO.[3]

Upwinding and Transport Models

For the first calculations, flow solutions about a 1-m sphere are generated and compared using GASP, GIANTS, and LAURA at the 1000-s conditions from Table 2 on an identical grid. All subsequent sphere calculations utilize the 1000-s conditions. The wall boundary condition is fixed at 2500 K, and the surface is noncatalytic to atomic recombination. A five-species chemistry model is employed.

In Figs. 1 and 2, the effects of various upwinding schemes on the flow and heat transfer rate are described. Figure 1 is a plot of the U velocity, temperature, and pressure along the stagnation line. The major difference between the flow solvers resides in the upwind formulations, which affect the shock capturing capabilities and numerical dissipation of each method. The upwind formulations for the various codes are listed. The calculations are in good agreement except in the shock region. The first-order Van Leer method is the

Table 2 Benchmark trajectory conditions

Time, s	Altitude, km	Velocity, km/s	Density, kg/m^3	T_∞, K
1000	72.0	6.4602	7.15×10^{-5}	216.7
1300	64.0	4.8497	4.19×10^{-4}	253.8

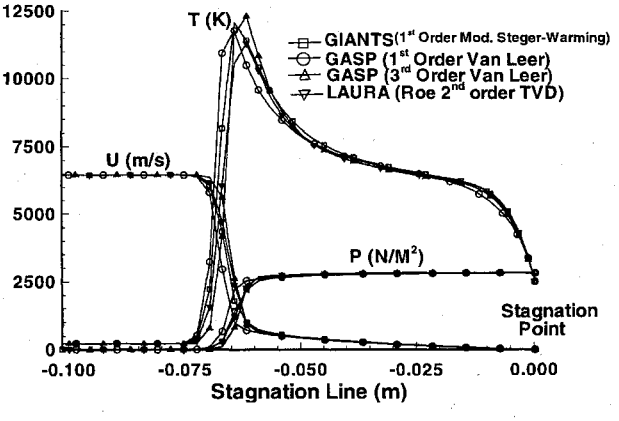

Fig. 1 Comparison of stagnation line flow properties for various codes. Wall boundary conditions: noncatalytic, T_w = 2500 K.

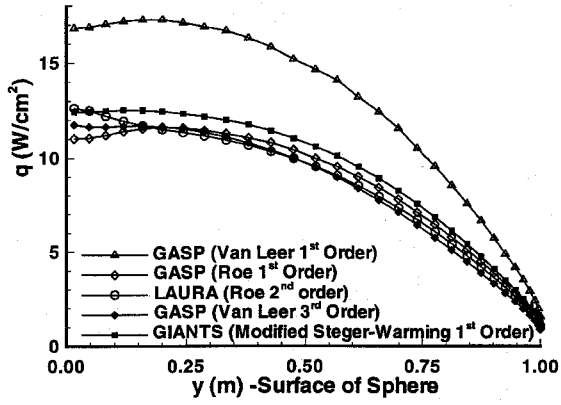

Fig. 2 Code to code comparison using various upwind methods on heat transfer. Wall boundary conditions: noncatalytic wall, T_w = 2500 K.

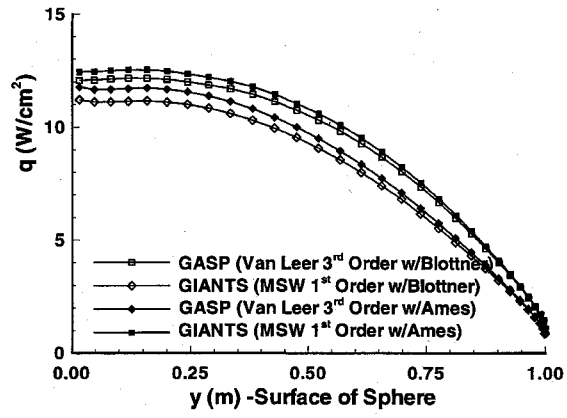

Fig. 3 Effect of transport model on heat transfer. Boundary conditions: noncatalytic wall, T_w = 2500 K.

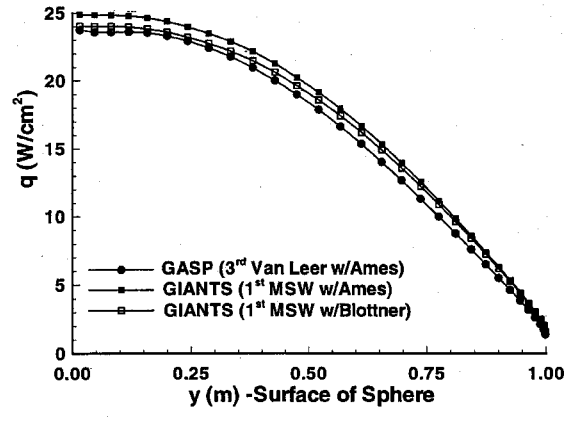

Fig. 4 Effects of transport model and catalycity on heat transfer. Wall boundary conditions: T_w = 2500 K, 2% catalytic to N recombination.

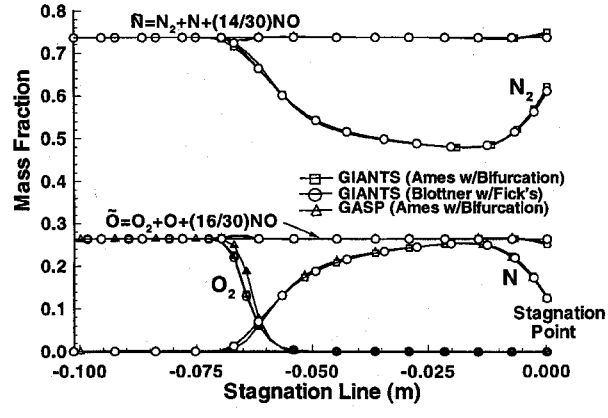

Fig. 5 Effect of transport model on stagnation line mass fractions. Boundary conditions: T_w = 2500 K, 2% catalytic to N recombination.

most dissipative upwinding scheme. It predicts the largest shock standoff distance and disagrees with the other methods in thermal boundary layer.

Figure 2 is a plot of the surface heat transfer using the various upwind schemes. It can be seen that the numerically dissipative first-order Van Leer method is inadequate for heat transfer calculations. The first-order modified Steger–Warming is slightly more dissipative and generates a slightly higher heat transfer than the other schemes. The higher-order methods, Roe with a second-order TVD scheme and Van Leer with a third-order MUSCL variable extrapolation, are in good agreement except near the stagnation point.

The divergence in the solutions near the stagnation point, which can be seen for both the first- and second-order Roe solutions is the result of eigenvalues in the Roe scheme approaching zero near the axis of symmetry. For blunt body flows at high Mach numbers, the zero eigenvalue problem can result in divergent or nonphysical solutions. To correct this problem, an eigenvalue limiter can be added to the Roe scheme,[11,23] which increases the numerical dissipation in the stagnation region. An eigenvalue limiter produces the higher stagnation heat transfer observed for the LAURA calculation. As a result of the problem with Roe's scheme around blunt bodies, subsequent GASP solutions in this work will employ the third-order Van Leer method. For heating, the method is about as dissipative as the second-order Roe scheme and does not produce as much difficulty around the axis of symmetry as the Roe scheme.

Next, in Figs. 3–5, the effects of transport algorithms and modeling are examined. Figure 3 is a plot of the surface heat transfer using two transport models for GIANTS and GASP. The Blottner model refers to the Blottner curve fits for species viscosity, which are used in conjunction with Wilke's mixing rule and Fick's law using a constant Schmidt number of 0.52. The Ames model uses the formulations in Ref. 14 and the transport data from Ref. 15 with a bifurcation approximation. It can be seen in the figure that using the Ames model for GIANTS or GASP leads to slightly higher heat transfer rates for the noncatalytic boundary conditions. The effect of the transport models on the flow solution is undiscernible and is not shown.

Figure 4 is a plot of the surface heat transfer with a wall that is 2% catalytic to nitrogen recombination. The surface catalycity leads to significantly higher heat transfer. Again, using the Ames transport model with bifurcation slightly increases the heat transfer. The difference in heating between the GASP and GIANTS solution is similar to the result using the noncatalytic boundary condition shown in Fig. 2.

Figure 5 is plot of the species and elemental mass fractions along the stagnation line for the calculations shown in Fig. 4. The GIANTS and GASP solutions using the Ames transport model are in good agreement. A difference between using Fick's law with a constant Schmidt number and a bifurcation approximation can be seen in the elemental mass fractions, $\tilde{N}$ and $\tilde{O}$. Using a constant Schmidt number, the elemental mass fractions remain constant. These values are straight lines. However, a bifurcation approximation allows for elemental separation, which more closely models the Knudsen layer near the surface of the vehicle.[24] The separation effect, although small for the conditions considered, should be more pronounced with increasing rarefication.

Grid Resolution and Heat Transfer Convergence

In the next set of calculations, the effects of grid resolution and distribution on the magnitude and convergence of the heat transfer rate are examined. Calculations are carried out on hemispheres with nose radii of 5 m and 30 cm. The wall is assumed to be noncatalytic with a fixed temperature of 1500 K. All of the flow solutions employ the Ames transport model.

In Figs. 6 and 7, the effects of grid distribution on the heat transfer rate and flow solution are examined for the 5-m sphere. Figure 6 is a plot of surface heating for various grids using GASP. Two grids with 30 cells along the body and 80 cells normal to the body

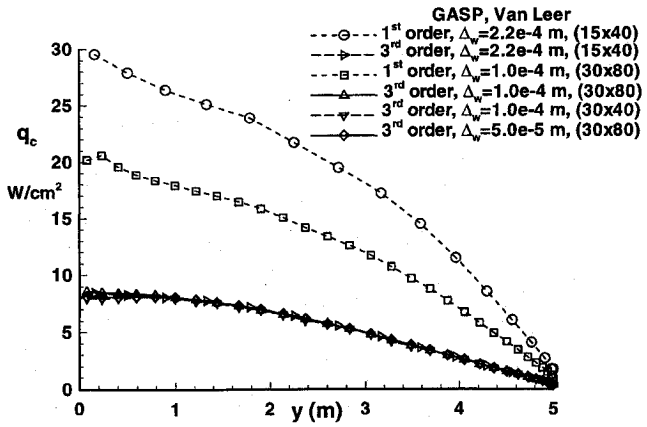

Fig. 6 Surface heating for various grid distributions. Boundary conditions: noncatalytic, T_w = 1500 K, 5 m sphere.

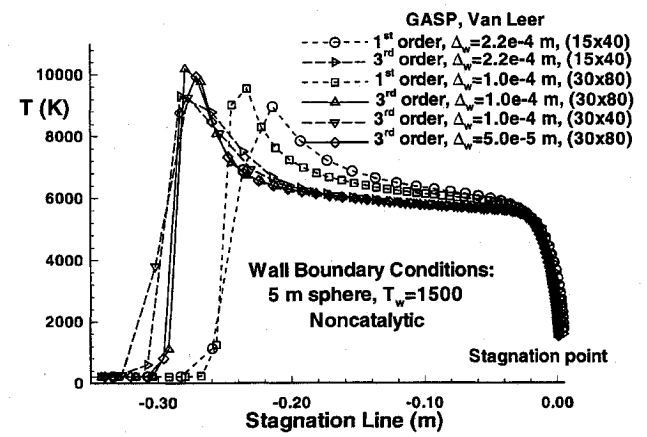

Fig. 7 Effect of grid distribution on shock standoff.

were generated with initial cell widths at the stagnation point Δ_w of 5.0×10^{-5} (m) and 1.0×10^{-4} (m). The (15 × 40) grids were obtained by removing every other point in the tangential and the normal directions from the (30 × 80) grids. The (30 × 40) grid was obtained by removing only points in the normal direction. As seen in Fig. 2, the first-order Van Leer is inadequate for predicting heat transfer. The first-order scheme is extremely sensitive to grid resolution. However, the predicted heat transfer using the third-order scheme is relatively insensitive to the grid resolution. Similar results are obtained on the coarsest and finest meshes.

Figure 7 is a plot of the temperature along the stagnation line for the various calculations. For the first-order scheme, the shock standoff distance is very sensitive to the grid resolution. However, for the third-order cases, the shock standoff distance is similar for all of the calculations. On the coarse grids, the shock is smeared and the peak temperature is reduced. Thus, it can be concluded from Figs. 6 and 7 that an adequate prediction of convective heat transfer can be obtained on a coarse grid using third-order Van Leer as long as the boundary layer is adequately resolved. For the third-order scheme, smearing the shock seemed to minimally affect the predicted heat transfer rate. For calculations in this work, the boundary layer is considered resolved if the change in temperature from the first cell center to the wall is on the order of 20 K or less.

In Figs. 8–11, grid resolution effects and the convergence of the heat transfer and overall numerical method are examined for a 30-cm hemisphere. Two (30 × 80) grids with Δ_w of 1.0×10^{-4} (m) and 5.0×10^{-6} (m) at the stagnation point are used. Again, the (30 × 40) grids are obtained by removing every other point in the normal direction. The ratio of Δ_w/R_n, $1.0 \times 10^{-4}/0.30$, is much larger than in the previous calculation. Thus, the flow gradients over the sphere are increased, and the effects of the initial spacing on the heating should be more pronounced.

Figure 8 is a plot of surface heating using the four grids. The difference in heating predicted on the finest and coarsest is grids is

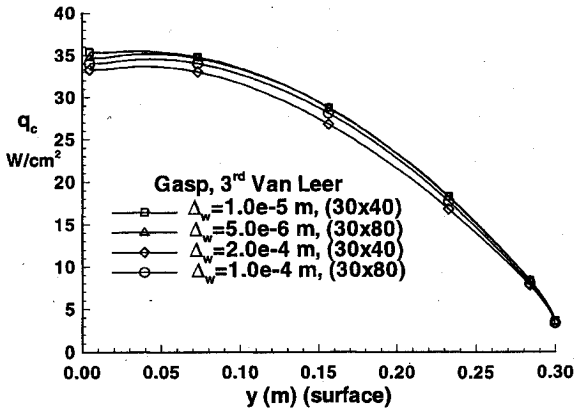

Fig. 8 Grid resolution effects for 30-cm hemisphere. Wall boundary conditions: T_w = 2500 K, noncatalytic, R_n = 30 cm.

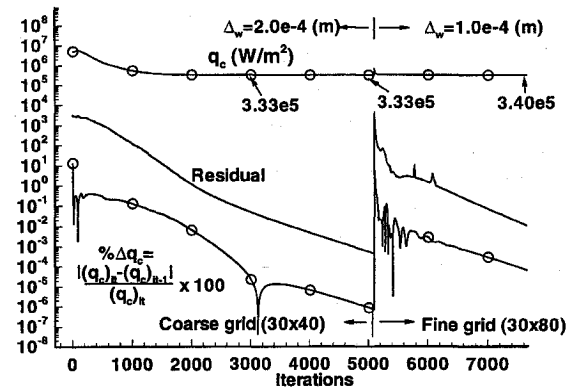

Fig. 9 GASP stagnation heating and residual convergence rates for coarse spacing. 30 cm sphere, T_w = 1500 K, noncatalytic wall, GASP, third Van Leer.

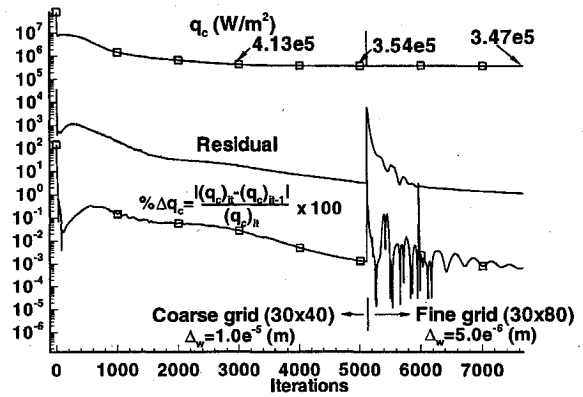

Fig. 10 GASP stagnation heating and residual convergence rates for fine spacing. 30 cm sphere, T_w = 1500 K, noncatalytic wall, GASP, third Van Leer.

about 5% at the stagnation point. However, the initial grid spacing for the finest grid is 40 times smaller than the coarsest grid. The spread in the predicted heating values for the rest of the cases is about 3% or less.

Figures 9 and 10 are plots of the stagnation heat transfer rate, residual, and percent change in the heating ($\%\Delta q_c$) as a function of iteration on the various grids using GASP. The calculations on the (30 × 80) grids were started using the (30 × 40) results. It can be seen in Fig. 9 that the slope of the $\%\Delta q_c$ curve tracks closely with the slope of the residual. By 3000 iterations, the residual on the coarse grid has dropped by four orders of magnitude and $\%\Delta q_c$ is about 1/10,000. At 5000 iterations, a solution was started on the fine grid. After 2500 iterations, $\%\Delta q_c$ is about 1/10,000. In Fig. 10, the previous calculation is repeated on the grids with the smaller initial stagnation point spacing. With more points in the boundary layer,

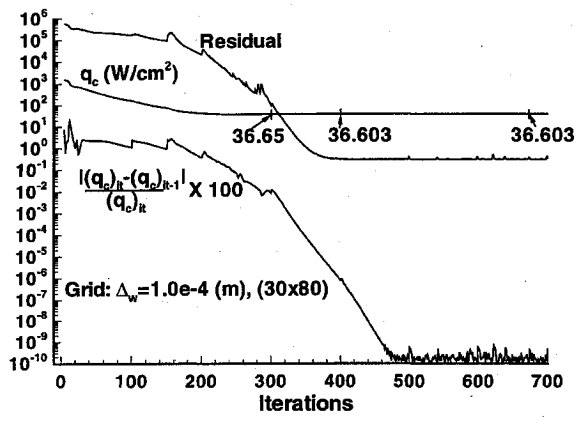

Fig. 11 GIANTS stagnation heating and residual convergence rates for coarse spacing. 30 cm sphere, T_w = 1500 K, noncatalytic wall, GIANTS, first MSW.

the slopes of both the residual curve and $\%\Delta q_c$ curve are reduced. Thus, the number of iterations needed to obtain a converged heating solution is increased.

Comparing the results of Figs. 8–10, it can be seen that a trade-off exists between computational cost and grid refinement in the boundary layer using GASP. More resolution in the boundary layer significantly increases the computational cost but only marginally increases the accuracy of the heating calculation. For a sphere, the computational cost is not a strong factor. However, for calculations over three-dimensional RLV configurations,[2–4] the trade between computational cost and boundary-layer resolution is critical. Further, comparing the results of the 5-m and 30-cm sphere calculations, it can be concluded that for heating the importance of grid resolution in the boundary layer decreases as the flow gradients decrease. Thus, in some cases, the penalty for using a coarse grid may not be large.

Finally, the heating convergence rate is calculated using GIANTS on the (30 × 80) grid with $\Delta_w = 1.0 \times 10^{-4}$. The results are plotted in Fig. 11. It can be seen that a converged heating solution is obtained in about 350 iterations. For this calculation, the computational cost of using GIANTS is much less than GASP. These results demonstrate the superiority of the Gauss–Seidel line algorithm for flows in which there is a preferred direction such as axisymmetric blunt body flows. Unfortunately, for three-dimensional calculations, the Gauss–Seidel line relaxation method is not directly applicable. Conclusions from this comparison should be made with the caution. The purpose of the comparison with GIANTS was to illustrate some of the limitations of the three-dimensional methodology. A faster solution could be obtained with GASP using an option that mimics the line relaxation technique employed in GIANTS. However, like the Gauss–Seidel technique, this method is not practical for three-dimensional calculations. Since the purpose was to benchmark methods applicable RLVs, the slower GASP methodology was employed.

Material-Dependent Flow Effects

Finally, flow solutions for a small three-dimensional geometry are generated to illustrate some phenomena using actual TPS materials. Figure 12 is the computational mesh around the nose of a SSTO vehicle.[3] The vehicle enters the atmosphere at a 40 deg angle of attack and is symmetric about the x–z plane. The conditions for the calculations are the 1000- and 1300-s values listed in Table 2. To determine whether the methodology used for the axisymmetric sphere calculations is applicable for three-dimensional, angle-of-attack calculations, a calculation is performed with a noncatalytic surface and a fixed temperature of 1500 K. A heating history for the pitch plane is plotted in Fig. 13 for the 1300-s conditions. The heating solution on the leeward side converges fairly quickly in about 3400 iterations. The heating rate convergence at the stagnation point on the windward side is similar to the sphere results in Figs. 9 and 10. A converged heating solution requires about 7000 iterations. Oscillations in the heating solution near $z = 0$ are the result of the singular axis passing through this point.

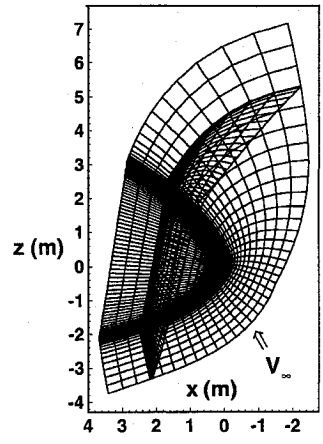

Fig. 12 Computational mesh around the nose of a SSTO vehicle. Grid for the nose of an access-to-space vehicle.

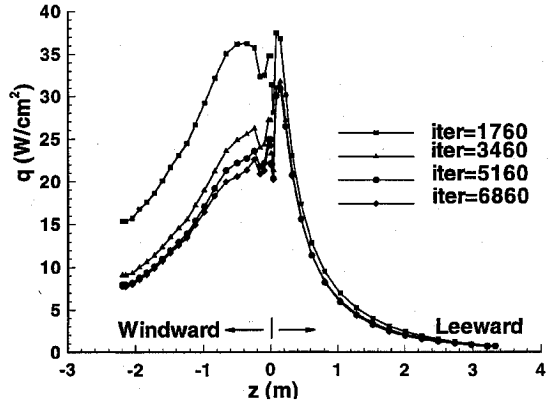

Fig. 13 Heating history for the pitch plane on the nose of an SSTO. Wall boundary conditions: T_w = 1500 K, noncatalytic, 1300 s.

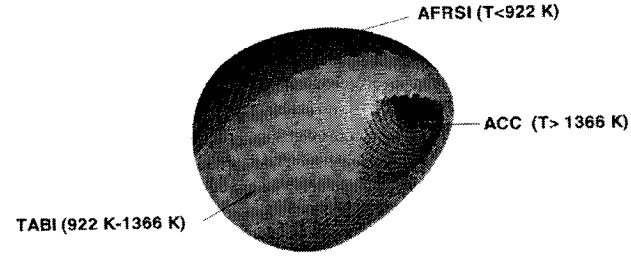

Fig. 14 Material mapping for the nose of an SSTO using the computational fluid dynamics solution at the 1000-s conditions. Surface boundary conditions: fully catalytic emissivity = 0.85.

In the next set of calculations, a material mapping is generated on the nose of an SSTO vehicle and the same material–fluid interaction effects are examined. Using a Fay and Ridell[25] stagnation point heat transfer analysis without catalytic effects, the peak heating location for a reference SSTO trajectory was the 1000-s condition.[1] Thus, a fully catalytic, radiative equilibrium boundary condition with a constant emissivity of 0.85 was employed to generate a conservative material mapping. The baseline materials and reusable temperature limits[1] were AFRSI[26] for surface temperature less than 922 K, tailorable advanced blanket insulation (TABI)[27] for temperatures between 922 and 1366 K, and advanced carbon-carbon (ACC)[28] for temperatures above 1366 K. Figure 14 is the material map for the nose of an SSTO at the 1000-s conditions using the baseline materials described. As expected, ACC is mapped to the hot stagnation region, AFRSI is on the leeward surface, and TABI is on the windward surface.

The material map from the previous solution was used for a calculation at the 1300-s conditions using a radiative equilibrium surface boundary condition. The emissivity and surface catalycity for each TPS material are a function of the radiative equilibrium wall temperature.[29,30] Figure 15 shows the material mapping from

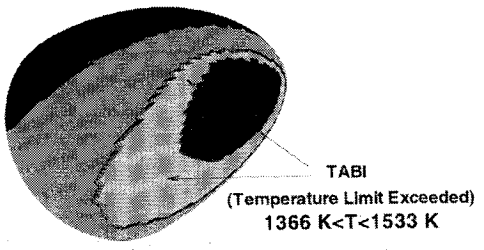

Fig. 15 Material map from 1000-s calculation with regions where the TPS material temperature limits are violated for the 1300-s calculation. Surface boundary conditions: material dependent catalyticity and emissivity.

the 1000-s calculation with regions where the resuable temperature limits for each material are violated. It can be seen that the temperature limits for TABI are exceeded in the stagnation region. The material map from the fully catalytic, 1000-s condition was inadequate for two reasons. First, when catalytic effects were included, it was found that the total predicted stagnation region heat transfer rates, convective and catalytic, are larger at the 1300-s conditions. Second, the surface catalycity is lower and the emissivity is higher for ACC than for uncoated TABI. These surface properties for ACC tend to lower the radiative equilibrium surface temperature relative to TABI. Further, the abrupt change in surface properties induces a significant temperature gradient at the interface between the two materials.[30]

An abrupt change in temperature at the boundaries between two materials with different properties can produce large local jumps in temperature that can thermally shock a vehicle's structure. On the early Shuttle flights, a number of tiles were sprayed with a highly catalytic overcoat. The change in catalycity produced a sharp rise in the local temperature.[31] As shown in Fig. 15, the maximum reuse temperature for TABI at the 1300-s conditions was exceeded in a region around the TABI–ACC interface. To determine whether this effect was a result of the overall higher level of heating at 1300 s or a result of the change in material properties at the TABI–ACC interface, a new material map was generated at 1300 s from a flow solution employing a fully catalytic wall boundary condition and a constant emissivity of 0.85. For comparison purposes, this case will be referred to as the fully catalytic solution. The map was generated using the maximum reuse temperatures for ACC, TABI, and AFRSI already described. Four flow solutions are generated with the new map in an attempt to quantify the effects of both the change in emissivity and surface catalycity at the ACC–TABI interface. The first solution is generated using the experimentally determined values of emissivity and catalycity for ACC and TABI. It is assumed that surface properties for TABI and AFRSI are the same. For the second solution, to separate out the effects of emissivity and to compare with the fully catalytic solution, the previous calculation was repeated with a constant emissivity of 0.85 for all of the materials. For the third solution, it is assumed that ACC is noncatalytic, $\gamma = 0$, and the TABI and AFSRI are fully catalytic, $\gamma = 1$, to atomic recombination. For this case, the actual emissivities of ACC and TABI are employed. Finally, for the fourth solution, the previous conditions are repeated with a constant emissivity of 0.85 for all of the materials.

Figure 16 is a plot of temperature contours along the windward and leeward centerlines on the nose of an SSTO for the surface conditions described in the preceding paragraph. Large jumps in temperatures occur at the boundaries between ACC and TABI. The largest jump occurs for the case where it is assumed that ACC is noncatalytic, TABI is fully catalytic, and the emissivity is material dependent. The emissivity of uncoated TABI is lower than that of ACC. It can be seen in the figure that this set of conditions predicts a temperature at the ACC–TABI interface that is higher than the fully catalytic solution with a constant emissivity of 0.85. Some explanations for this effect are as follows. First, because the ACC was assumed to be noncatalytic, a higher concentration of atoms exists at the ACC–TABI interface than for the fully catalytic conditions. The excess atoms are quickly recombined producing a large temperature jump. Second, as can be seen in Eq. (6), the recombination rate of atoms at the surface increases with increasing temperature,

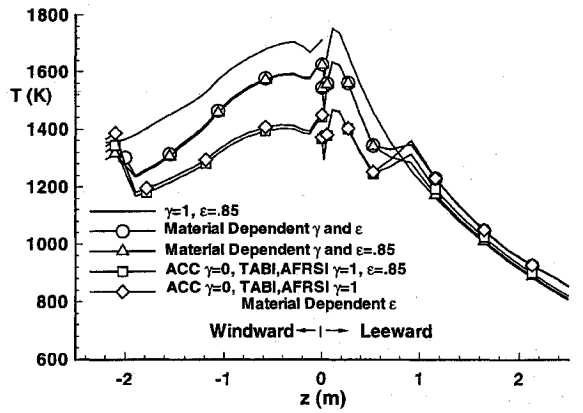

Fig. 16 Influence of the TPS material properties on the surface temperature profiles.

which would tend to raise the surface temperature. Finally, decreasing emissivity will raise the surface temperature for a given heat transfer rate. This effect also increases the recombination rate of atoms at the surface. Fortunately, the recombination rate of atoms at the surface is limited by diffusion. The effect of emissivity was determined by running the noncatalytic–fully catalytic conditions with a constant emissivity of 0.85 for all of the materials. Since the emissivity value of 0.85 is higher than the material-dependent value for TABI, the temperature jump is slightly lowered. The calculation using material-dependent properties for the catalycity and emissivity of ACC, TABI, and AFRSI, denoted by circles, predicts temperatures on the ACC that are higher than the previous calculations and the temperature gradient at the ACC–TABI interface is lower. This result was expected because a finite catalytic rate was used for ACC. However, the maximum temperature at the interface is still higher than the fully catalytic solution. The solution denoted by the diamonds produced the highest peak temperature at the interface, followed by the circles, squares, and triangles. Again, using a constant emissivity of 0.85 tends to lower the temperature. Finally, note that a jump in temperature was not observed at the TABI–AFRSI interface on the leeward side because the surface properties of TABI and AFRSI are the same.

The temperature plots shown in Fig. 16 demonstrate the importance of including accurate material properties in flow simulations geared toward TPS material selection and sizing. The sharp temperature gradients at the ACC–TABI interface produced surface temperatures that were higher than the conservative fully catalytic solution. Thus, the reusable temperature limits for the material mapping generated from the fully catalytic solution were locally violated.

Concluding Remarks

A study was made to identify and develop better methods for TPS material selection and sizing on RLVs. For validation purposes, hypersonic flow solutions with finite rate chemistry about a sphere were calculated and compared using three flow solvers, GASP, GIANTS, and LAURA. The methods predicted similar flow solutions except in the shock. Discrepancies in the shock region were attributed to the different upwind formulations used in each code.

For calculating heat transfer around spheres, a third-order Van Leer scheme produced the best results. It compared favorably with a second-order TVD Roe scheme. Further, instabilities associated with Roe's scheme near stagnation points were not as great for the Van Leer method. A first-order Van Leer scheme was found to be inadequate for calculating heat transfer.

Two transport models, Blottner with Fick's law and a constant Schmidt number and an Ames model with a bifurcation approximation, were compared. For the flow conditions considered, it was found that using the Ames model resulted in a slightly higher heat transfer rate. This result was observed using a Steger–Warming or Van Leer upwind formulation and for a noncatalytic or catalytic surface. It was observed that the bifurcation method allows for separation of the atomic mass fractions in the boundary layer.

In grid resolution and distribution studies over 5-m and 30-cm nose radii spheres using GASP, the Van Leer scheme with third-order

MUSCL extrapolation was found to produce consistent heating predictions as long the thermal boundary layer was adequately resolved. The shock layer could be significantly smeared without affecting the prediction heat transfer rate. In examining the convergence of the heat transfer rate, a tradeoff was identified between resolution in the boundary layer and computational cost. Increasing the resolution of the boundary layer was found to significantly increase the computational cost of the calculation. However, the accuracy on the heat transfer prediction was minimal.

A number of three-dimensional calculations were performed over the nose of a SSTO rocket using GASP. The convergence history of the heat transfer rate was found to agree with the sphere calculations. A material map for the nose of an SSTO was generated employing the reuse temperatures of ACC, AFRSI, and TABI. It was found that the surface properties of a chosen TPS material strongly influence predicted heat transfer results. Abrupt changes in TPS surface catalycity and emissivity produced significant jumps in temperatures at the material interfaces. These temperatures were locally higher than the temperatures predicted employing conservative fully catalytic surface conditions. Thus, these calculations illustrate the importance of including accurate surface boundary conditions for flow simulations geared toward TPS material selection and sizing.

Acknowledgments

The authors would like to acknowledge Sal Riccitiello, Jeff Bowles, Y.-K. Chen, and the members of the Thermal Protection Materials and Systems Branch in general for many helpful conversations on various TPS topics. Also, the authors would like to thank Peter Gnoffo of the Aerothermodynamics branch at NASA Langley Research Center for contributing a sphere solution using LAURA.

References

[1]Anon., "Access to Space, Advanced Technology Team, Final Report: Volumes 1–4," NASA, July 1993.

[2]Chen, Y.-K., Henline, W. D., Olynick, D. R., and Palmer, G. E., "Three-Dimensional Hypersonic Flowfields and Heating Analysis over the DC-3 Vehicle," AIAA Paper 95-2081, June 1995.

[3]Henline, W. D., Palmer, G. E., Olynick, D. R., and Chen, Y.-K., "Aerothermodynamic Heating Analysis and Heatshield Design of an SSTO Rocket Vehicle for Access-to-Space," AIAA Paper 95-2079, June 1995.

[4]Palmer, G. E., Henline, W. D., Olynick, D. R., and Chen, Y.-K., "Heating Analysis of a Lifting Body Single-Stage-to-Orbit Vehicle," AIAA Paper 95-2080, June 1995.

[5]Chen, Y.-K., Henline, W. D., and Tauber, M. E., "Trajectory Based Heating and Ablation Calculations for Mars/Pathfinder Aeroshell," *Journal of Spacecraft and Rockets*, Vol. 32, No. 2, 1995, pp. 225–230.

[6]Hirsch, C., *Numerical Computation of Internal and External Flows, Vol. 2: Computation Methods for Inviscid and Viscous Flows*, 1st ed., Wiley, New York, 1990, pp. 493–583.

[7]Cleland, J., and Iannetti, F., "Thermal Protection System of the Space Shuttle," NASA CR-4227, June 1989.

[8]Gnoffo, P. A., Weilmuenster, K. J., and Alter, S. J., "Multiblock Analysis for Shuttle Orbiter Re-entry Heating from Mach 24 to Mach 12," *Journal of Spacecraft and Rockets*, Vol. 31, No. 3, 1994, pp. 385–394.

[9]McGrory, D. M., Slack, D. C., Applebaum, M. P., and Walters, R. W., "GASP Version 2.2: User's Manual," AeroSoft, Inc., Blacksburg, VA, 1993.

[10]Gnoffo, P. A., Gupta R. N., and Shinn, J. L., "Conservation Equations and Physical Models for Hypersonic Air Flows in Thermal and Chemical Nonequilibrium," NASA TP-2867, Feb. 1989.

[11]Gnoffo, P. A., "An Upwind-Biased Point-Implicit Relaxation Algorithm for Viscous, Compressible Perfect-Gas Flows," NASA TP-2953, Feb. 1990.

[12]Olynick, D. R., Henline, W. D., Chamber, L. H., and Candler, G. V., "Comparisons of Coupled Radiative Flow Solutions with Project Fire II Flight Data," *Journal of Thermophysics and Heat Transfer*, Vol. 9, No. 4, 1995, pp. 586–594.

[13]Candler, G. V., "The Computation of Weakly Ionized Hypersonic Flows in Chemical Nonequilibrium," Ph.D. Thesis, Dept. of Aeronautics and Astronautics, Stanford Univ., Stanford, CA, June 1988.

[14]Gupta, R. N., Yos, J. M., Thompson, R. A., and Lee, K., "A Review of Reaction Rates and Thermodynamic and Transport Properties for an 11-Species Air Model for Chemical and Thermal Nonequilibrium Calculations to 30,000 K," NASA RP-1232, Aug. 1990.

[15]James Stallcop, private communication, Computational Chemistry Branch, NASA Ames Research Center, Moffett Field, CA, June 1993.

[16]Lee, J.-H., "Basic Governing Equations for the Flight Regimes of Aeroassisted Orbital Transfer Vehicles," *Thermal Design of Aeroassited Orbital Transfer Vehicles*, edited by H. F. Nelson, Vol. 96, Progress in Astronautics and Aeronautics, AIAA, New York, 1985, pp. 3–53.

[17]Bartlett, E. P., Kendal, R. M., and Rindal, R. A., "An Analysis of the Coupled Chemically Reacting Boundary Layer and Charring Ablator: Part IV— A Unified Approximation for Mixture Transport Properties for Multicomponent Boundary-Layer Applications," NASA CR-1063, June 1968.

[18]Desmeuzes, C., Duffa, G., and Dubroca, B., "Different Levels of Modelization for Diffusion Phenomena in Neutral and Ionized Mixtures," AIAA Paper 94–2412, June 1994.

[19]Wilke, C. R., "A Viscosity Equation for Gas Mixtures," *Journal of Chemical Physics*, Vol. 18, No. 4, 1950, p. 517.

[20]Blottner, F. G., Johnson, M., and Ellis, M., "Chemically Reacting Viscous Flow Program for Multi-Component Gas Mixtures," Sandia Labs., Rept. SC-RR-70-754, Albuquerque, NM, Dec. 1971.

[21]Milos, F. S., and Rasky, D. J., "Review of Numerical Procedures for Computational Surface Thermochemistry," *Journal of Thermophysics and Heat Transfer*, Vol. 8, No. 1, 1994, pp. 24–34.

[22]Stewart, D. A., Rakich, J. V., and Chen, Y.-K., "Flight Experiment Demonstrating the Effect of Surface Catalysis on the Heating Distribution over the Space Shuttle Heat Shield," *Orbiter Experiments (OEX) Aerothermodynamics Symposium*, edited by David A. Throckmorton, NASA CP-3248, Pt. 2, April 1993, pp. 677–702.

[23]Olynick, D. R., "A New LU-SGS Flow Solver for Calculating Reentry Flows," Ph.D Thesis, Dept. of Mechanical and Aerospace Engineering, North Carolina State Univ., Raleigh, NC, Dec. 1992.

[24]Olynick, D. R., Taylor, J. C., and Hassan, H. A., "Comparisons Between DSMC and the Navier–Stokes Equations for Reentry Flows," *Journal of Thermophysics and Heat Transfer*, Vol. 8, No. 2, 1994, pp. 251–258.

[25]Fay, J. A., and Ridell, F. R., "Theory of Stagnation-Point Heat Transfer in Dissociated Air," *Journal of Aerospace Sciences*, Vol. 25, No. 2, 1958, pp. 54–67.

[26]Sawko, P. M., and Goldstien, H. E., "Performance of Uncoated AFRSI Blankets During Multiple Space Shuttle Flights," NASA TM-103892, April 1992.

[27]Calamito, D. P., "Development of Tailorable Advanced Blanket Insulation for Advanced Space Transportation Systems," NASA CR-177444, April 1987.

[28]Williams, S. D., Curry, D. M., Chao, D., and Pham, V. T., "Analysis of the Shuttle Orbiter Reinforced Carbon-Carbon Oxidation Protection System," NASA TM-104792, June 1994.

[29]Chiu, S. A., and Pitts, W. C., "Reusable Surface Insulations for Reentry Spacecraft," AIAA Paper 91-0695, Jan. 1991.

[30]Stewart, D. A., Pallix, J., and Esfahani, L., "Surface Catalytic Efficiency of Candidate Ceramic Thermal Protection Materials for SSTO," NASA CDTM-20007, March 1995.

[31]Stewart, D. A., Rakich, J. V., and Lanfranco, M. J., "Catalytic Surface Effects on Space Shuttle Thermal Protection System During Earth Entry of Flights STS-2 Through STS-5," NASA CP-2283, March 1983.

K. J. Weilmuenster
Associate Editor